

Electronic Supplementary Information (ESI)

Maximizing the Utility of Single Atom Electrocatalyst on a 3D Graphene Nanomesh

*Kai Chi, Zhongxin Chen, Fei Xiao, Wei Guo, Wei Xi, Jing Liu, Huan Yan, Zheyue Zhang,
Jian Xiao, Jia Liu, Jun Luo, Shuai Wang*, Kian Ping Loh**

K. Chi, W. Guo, Z. Zhang, J. Xiao, Prof. F. Xiao, Prof. S. Wang

Key laboratory of Material Chemistry for Energy Conversion and Storage, Ministry of Education, School of Chemistry and Chemical Engineering, Huazhong University of Science and Technology, Wuhan, 430074, PR China.

Dr. Z. Chen, Dr. H. Yan, J. Liu, Prof. K. Loh

Department of Chemistry and Centre for Advanced 2D Materials (CA2DM), National University of Singapore, 3 Science Drive 3, Singapore 117543, Singapore.

Dr. W. Xi, J. Liu, Prof. J. Luo

Tianjin Key Laboratory of Advanced Functional Porous Materials and Center for Electron Microscopy, School of Materials Science and Engineering, Tianjin University of Technology, Tianjin 300384, China.

*Corresponding author: chmsamuel@hust.edu.cn (S. Wang); chmlhkp@nus.edu.sg

(K. P. Loh)

K.C., Z.C., F.X., and W.G. contributed equally to this work.

Supplementary Methods:

Preparation of VNGNMAs. The carbon cloth (CC) was immersed in an ethanol and 30% hydrogen peroxide mixture (v/v = 1:1) at 60 °C for 24 hours for activation, and then placed into 25 ml of NiCl₂·6H₂O (0.125M) and hexamethylenetetramine (0.25M) aqueous solution at 100 °C for 10 h. CC@Ni(OH)₂ was obtained after natural cooling, rinsed with deionized water and dry, and further dipped into a Tris aqueous solution containing dopamine (2 mg of dopamine per milliliter of 10 mM Tris(hydroxymethyl)aminomethane). The pH value of the buffer is ~ 8.5. After reaction for 24 h, CC@Ni(OH)₂ has been coated by a layer of PDA film, which was taken out from the solution and washed with deionized water. This step was repeated twice to give CC@Ni(OH)₂@PDA. Pyrolysis of PDA was conducted at 400 °C under Ar atmosphere for 2 h, followed by further treatment at 800 °C for 3 h. All the heating rates are 2 °C min⁻¹. Finally, as-obtained sample was soaked in 3 M HCl aqueous solution at 80 °C for 48 h to remove the remaining nickel particles to obtain VNGNMAs. The mass loading of VNGNMAs on carbon cloth is ≈0.7 mg cm⁻².

Preparation of VNGNMAs SAC catalysts. The synthesis of Pd₁ and Pt₁ SACs were performed in a viscous ALD flow reactor (Plasma-assisted ALD system, Wuxi MNT Micro and Nanotech Co., Ltd, China) by alternatively exposing VNGNMAs to Pd(hfac)₂ & MeCpPtMe₃ precursors and O₃ at 150 °C. Ultrahigh purity N₂ (99.99%) was used as carrier gas with a flow rate of 50 mL min⁻¹. The Pd & Pt precursors were heated at 100 °C to generate a high enough vapor pressure. The reactor and reactor

inlets were held at 150 and 120 °C respectively to avoid any precursor condensation. An *in-situ* thermal reduction of as-received VNGNMAs support was conducted at 300 °C for 5 min before performing Pd & Pt ALD. The timing sequence was 100, 120, 150, and 120 seconds for the Pd(hfac)₂ & MeCpPtMe₃ exposure, N₂ purge, O₃ exposure and N₂ purge, respectively. Conducting Pd & Pt ALD with 1 cycle allows for the synthesis of Pd₁-SAC VNGNMAs & Pt₁-SAC VNGNMAs. The mass loading of Pt and Pd is ≈22 μg cm⁻² and 6.4 μg cm⁻², respectively.

Materials Characterizations. The morphology and structure of products were characterized with a field-emission scanning electron microscope (FESEM, FEI, Nova NanoSEM 450). Transmission electron microscopy (TEM) and high-resolution TEM (HRTEM) images were obtained using a TECNAI G220 U-Twin instrument (Netherlands) operated at an acceleration voltage of 200 kV. Atomic resolution images and elementary mapping were acquired by an aberration-corrected JEOL ARM-200F system equipped with a cold field emission gun and an ASCOR probe corrector at 60 kV. The samples subjected to TEM measurements were ultrasonically dispersed in ethanol and drop-cast onto a carbon-coated 200-mesh copper grid which was then subsequently dried at room temperature. X-ray photoelectron spectroscopy (XPS) was performed on a Kratos-Axis spectrometer with monochromatic Al K_α (1486.71 eV) X-ray radiation (15 kV and 10 mA) and a hemispherical electron energy analyzer. X-ray diffraction (XRD) patterns were recorded using a diffractometer (X'Pert PRO, Panalytical B.V., Netherlands) equipped with a Cu K_α

radiation source ($\lambda = 1.5406 \text{ \AA}$). Raman spectra were measured on a confocal laser micro-Raman spectrometer (Thermo Fischer DXR, USA) equipped with a He-Ne laser of excitation of 532 nm. N_2 adsorption/desorption isotherms were measured on an accelerated surface area and porosimetry system (ASAP 2020) at 77 K. The specific surface areas were calculated using adsorption data by the Brunauer-Emmett-Teller method. Pore size distribution curves were computed from the desorption branches of the isotherms using the BJH method.

Electrochemical measurements. Electrochemical measurements were performed on an Autolab PGSTAT30 with a 3-electrodes cell using carbon rod and saturated calomel electrode (SCE), carbon cloth samples as the counter, reference and working electrodes, respectively. Linear sweep voltammetry was collected at a scan rate of 5 mV s^{-1} in $0.5 \text{ M H}_2\text{SO}_4$ at room temperature. All the potentials were calibrated to a reversible hydrogen electrode (RHE). For comparison, 20% Pt/C catalyst on carbon cloth was also prepared. A 2 mL homogeneous 20% Pt/C catalyst dispersion was obtained by sonication for 30 min, consisting of 10 mg Pt/C, 500 μL water, 100 μL 5% Nafion solution, and 1.4 mL ethanol. 125 μL of catalyst ink was then sprayed onto 1 cm^2 carbon cloth for test. For peroxide reduction reaction (PRR) and electrochemically active surface areas (ECSAs) tests, the working electrode with the mass loading of $\sim 0.70 \text{ mg cm}^{-2}$ was prepared via dropping 140 μL of the ink, which was prepared via dispersing 5 mg of the $\text{Pt}_1\text{-VNVGMA}$ s powder into 20 μL of Nafion (5 wt%) and 0.98 mL of ethanol on the carbon cloth. The ECSAs were estimated by a series of

cyclic voltammetry measurements performed with various scan rates (5, 10, 15, 20, 25, 30, 35 and 40 mV s⁻¹) in 0.06-0.16 V versus RHE region. Hydrogen peroxide reduction reaction performance were evaluated by CV curves with different concentration of H₂O₂ in 0.5M H₂SO₄ solution at the scan rate of 10 mV s⁻¹.

***In-situ* TEM observation of VNGNMAs Formation.** The *in-situ* TEM imaging experiments were carried out on FEI Talos F200X at 200 kV in the Center for Electron Microscopy at Tianjin University of Technology. A DENSsolutions *in-situ* heating holder with a gas cell was used for the *in-situ* experiments. The 400°C-treated sample was dispersed in ethanol and sonicated before re-dispersing onto the heating chip of the gas cell. During the observation, Ar was introduced into the gas cell at a flow rate of 5 ml per minute, and the sample was heated from room temperature to the desired temperature using a rate of 10 °C min⁻¹.

Turnover frequency (TOF) calculations.

The per-site TOF value was calculated according to the following equation:

$$\text{TOF}(\text{H}_2/\text{s}) = \frac{\# \text{ total hydrogen turnovers per geometric area}}{\# \text{ active sites per geometric area}}$$

The total number of hydrogen turn over events is calculated from the current density using the following conversion:

$$\left(\frac{j}{\text{cm}^2} \right) \left(\frac{1 \text{ A}}{1000 \text{ mA}} \right) \left(\frac{1 \text{ C/s}}{1 \text{ A}} \right) \left(\frac{1 \text{ mol } e^-}{96485.3 \text{ C}} \right) \left(\frac{1 \text{ mol } \text{H}_2}{2 \text{ mol } e^-} \right) \left(\frac{6.02214 \times 10^{23} \text{ molecules } \text{H}_2}{1 \text{ mol } \text{H}_2} \right)$$

$$= 3.12 \times 10^{15} \frac{H_2/s}{cm^2} \text{ per } \frac{mA}{cm^2}$$

The number of active sites in Pt₁ SAC-VNGNMAs, Pd₁ SAC-VNGNMAs and Pt/C catalyst was calculated from the mass loading on the carbon cloth, the Pt, Pd contents and atomic weight, assuming each Pt or Pd center accounts for one active site:

Pt₁ SAC-VNGNMAs:

#active sites =

$$\begin{aligned} & \left(\frac{\text{Pt atoms loading per geometric area (x g/cm}^2)}{\text{Pt } M_w(\text{g/mol})} \right) \left(\frac{6.02214 \times 10^{23} \text{ Pt atoms}}{1 \text{ mol Pt}} \right) \\ & = \left(\frac{22 \mu\text{g/cm}^2}{195.08 \text{ g/mol}} \right) \left(\frac{6.02214 \times 10^{23} \text{ Pt atoms}}{1 \text{ mol Pt}} \right) \\ & = 6.79 \times 10^{16} \text{ Pt sites per cm}^2 \end{aligned}$$

The current density from the LSV polarization curve can be converted into TOF values according to:

$$\text{TOF} = \left(\frac{3.12 \times 10^{15}}{6.79 \times 10^{16}} \times |j| \right) = 0.0459 \times |j|$$

Pd₁ SAC-VNGNMAs:

#active sites =

$$\begin{aligned} & \left(\frac{\text{Pd atoms loading per geometric area (x g/cm}^2)}{\text{Pd } M_w(\text{g/mol})} \right) \left(\frac{6.02214 \times 10^{23} \text{ Pd atoms}}{1 \text{ mol Pd}} \right) \\ & = \left(\frac{6.4 \mu\text{g/cm}^2}{106.42 \text{ g/mol}} \right) \left(\frac{6.02214 \times 10^{23} \text{ Pd atoms}}{1 \text{ mol Pd}} \right) \\ & = 3.63 \times 10^{16} \text{ Pd sites per cm}^2 \end{aligned}$$

$$\text{TOF} = \left(\frac{3.12 \times 10^{15}}{3.63 \times 10^{16}} \times |j| \right) = 0.0859 \times |j|$$

Pt/C:

$$\begin{aligned}
& \left(\frac{\text{Pt/C catalyst loading per geometric area (x g/cm}^2\text{)} \times \text{Pt wt}\%}{\text{Pt } M_w(\text{g/mol})} \right) \\
& \left(\frac{6.02214 \times 10^{23} \text{ Pt atoms}}{1 \text{ mol Pt}} \right) \\
\text{\#active sites} = & \\
= & \left(\frac{6.25 \mu\text{g/cm}^2 \times 20\%}{195.08 \text{ g/mol}} \right) \left(\frac{6.02214 \times 10^{23} \text{ Pt atoms}}{1 \text{ mol Pt}} \right) \\
= & 3.858 \times 10^{17} \text{ Pt sites per cm}^2 \\
\text{TOF} = & \left(\frac{3.12 \times 10^{15}}{3.858 \times 10^{17}} \times |j| \right) = 0.00808 \times |j|
\end{aligned}$$

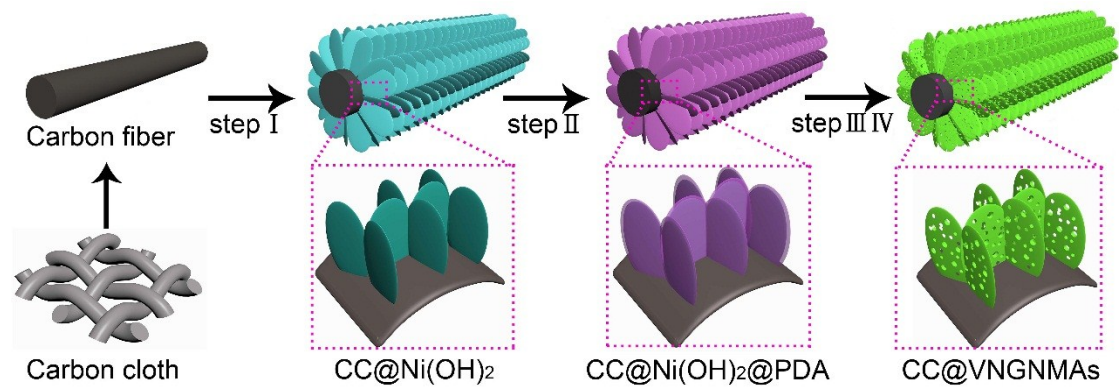


Figure S1. Schematic illustration of the fabrication of VNGNMA. The vertical structure is inherited from Ni(OH)₂ plates by the self-polymerization of PDA and subsequent pyrolysis of PDA into graphene.

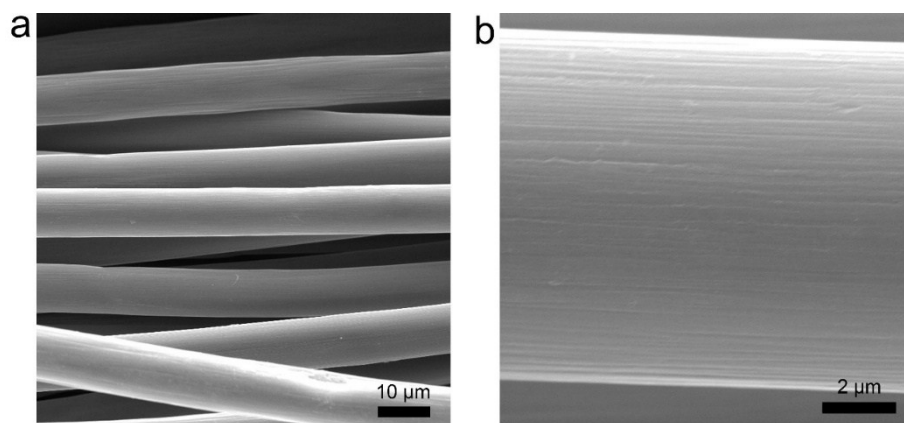


Figure S2. SEM images of pure carbon cloth.

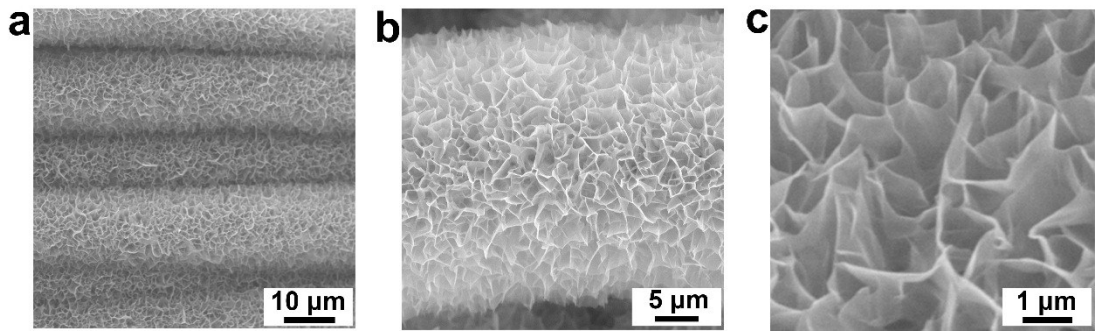


Figure S3. SEM images of CC@Ni(OH)₂.

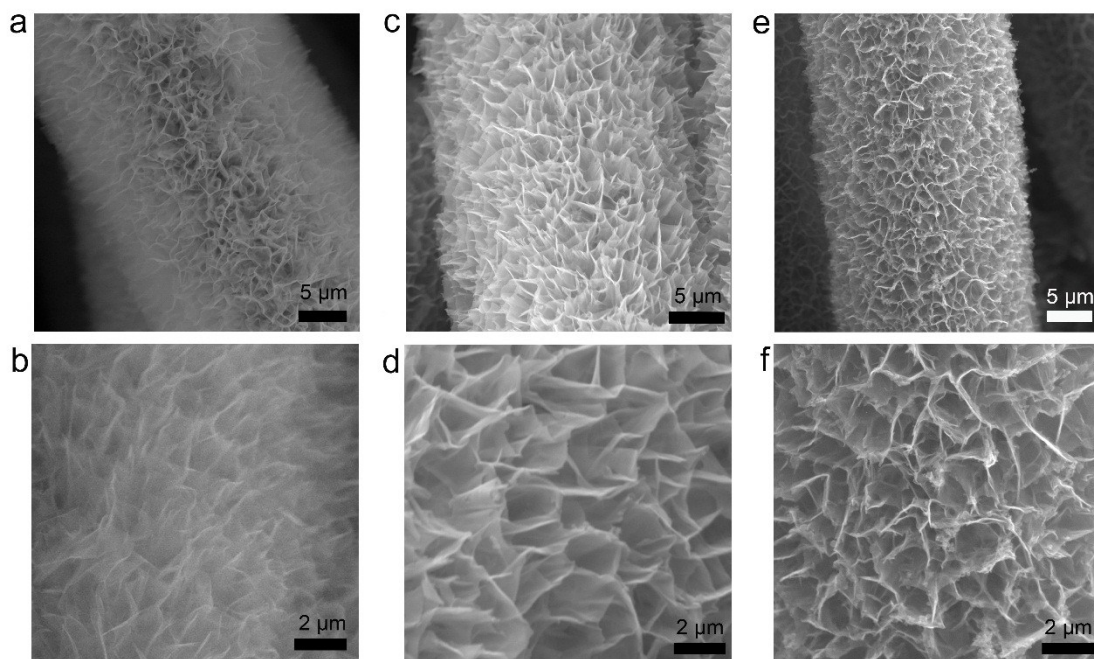


Figure S4. SEM images of CC@Ni(OH)₂@PDA (a,b), the annealed 400 °C (c,d) and 800 °C (e,f) samples.

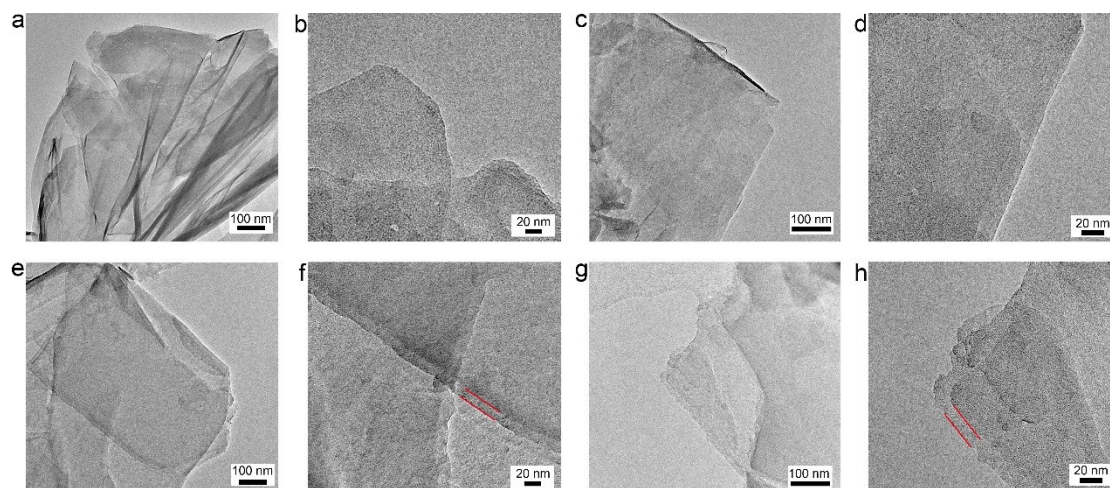


Figure S5. TEM images of Ni(OH)_2 (a-d) and $\text{Ni(OH)}_2@PDA$ nanosheets (e-h).

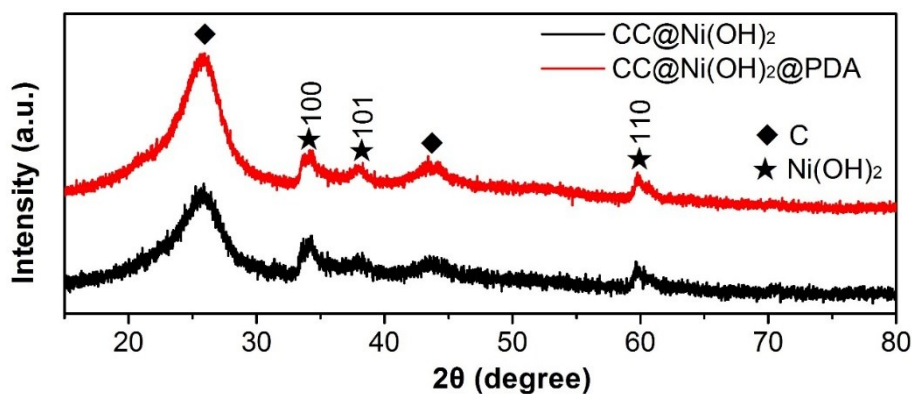


Figure S6. The XRD patterns of the CC@Ni(OH)_2 and $\text{CC@Ni(OH)}_2\text{@PDA}$.

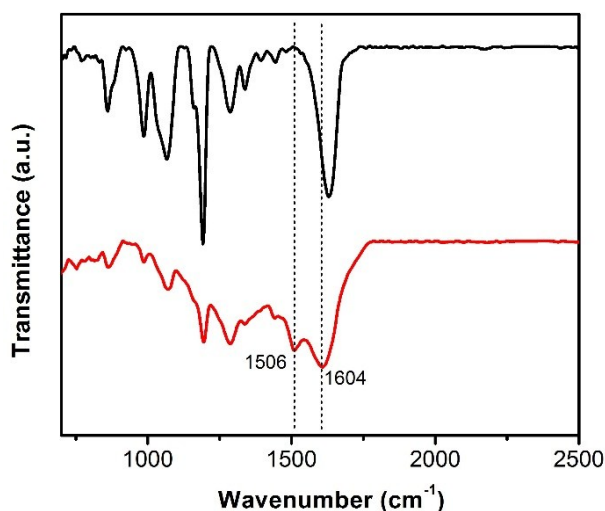


Figure S7. FTIR spectra of CC@Ni(OH)_2 and $\text{CC@Ni(OH)}_2\text{@PDA}$ samples.

We have provided the evidences on successful coating of the desired substance (*e.g.*, the uniform coating of dopamine) from SEM, TEM, XRD and FTIR spectroscopy. From the SEM images, we can see that $\text{CC@Ni(OH)}_2\text{@PDA}$ retains the nanosheets array structure of original CC@Ni(OH)_2 in Figure S4. It is observed from the TEM image that the PDA is uniformly coated on the surface of the Ni(OH)_2 nanosheet, and the thickness of the PDA layer is about 15 nm (Figure S5). Fourier transform infrared

spectroscopy (FTIR) further verifies the successful coating of PDA. As depicted in Figure S7, the revealed characteristic peaks at 1,506 and 1,604 cm^{-1} are consistent with the indole or indoline structures of PDA (Ref. *Science*, 2007, 318, 426-430). Meanwhile, these samples exhibit typical XRD patterns of $\text{Ni}(\text{OH})_2$ (Ref. *ACS Nano*, 2014, 8, 11280-11289), and the coating of PDA does not affect the crystal structure of $\text{Ni}(\text{OH})_2$ (Figure S6).

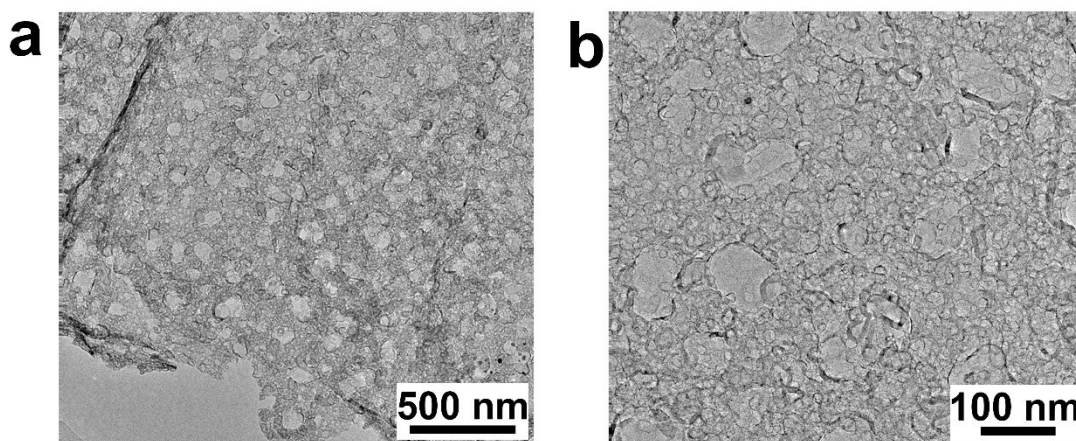


Figure S8. TEM images of VNGNMAs.

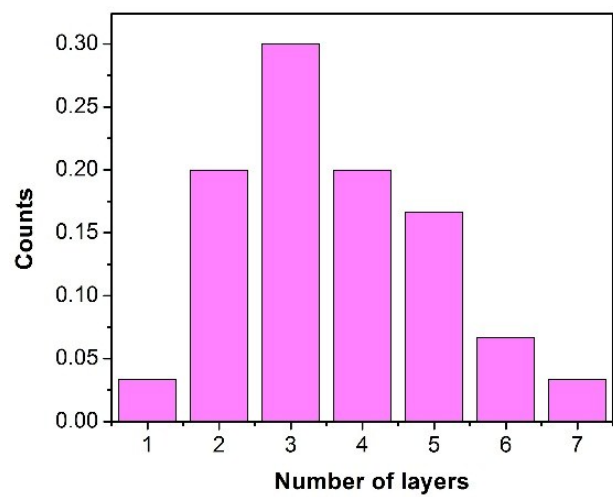


Figure S9. layer number distribution of VNGNMAs.

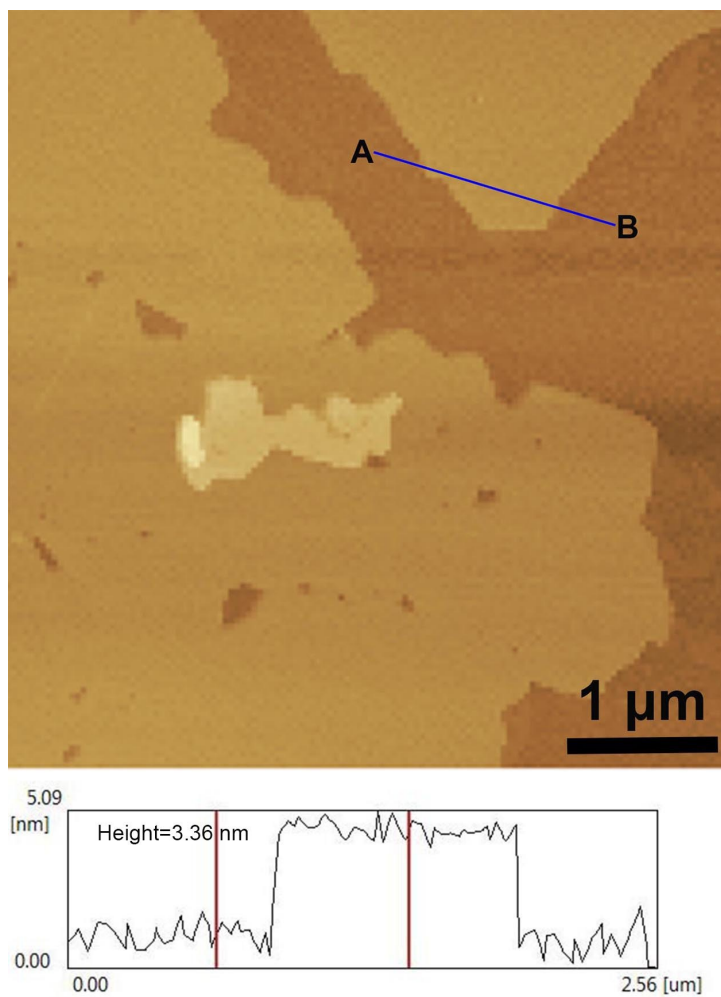


Figure S10. AFM image of VNGNMA and the corresponding height profile along a line scan.

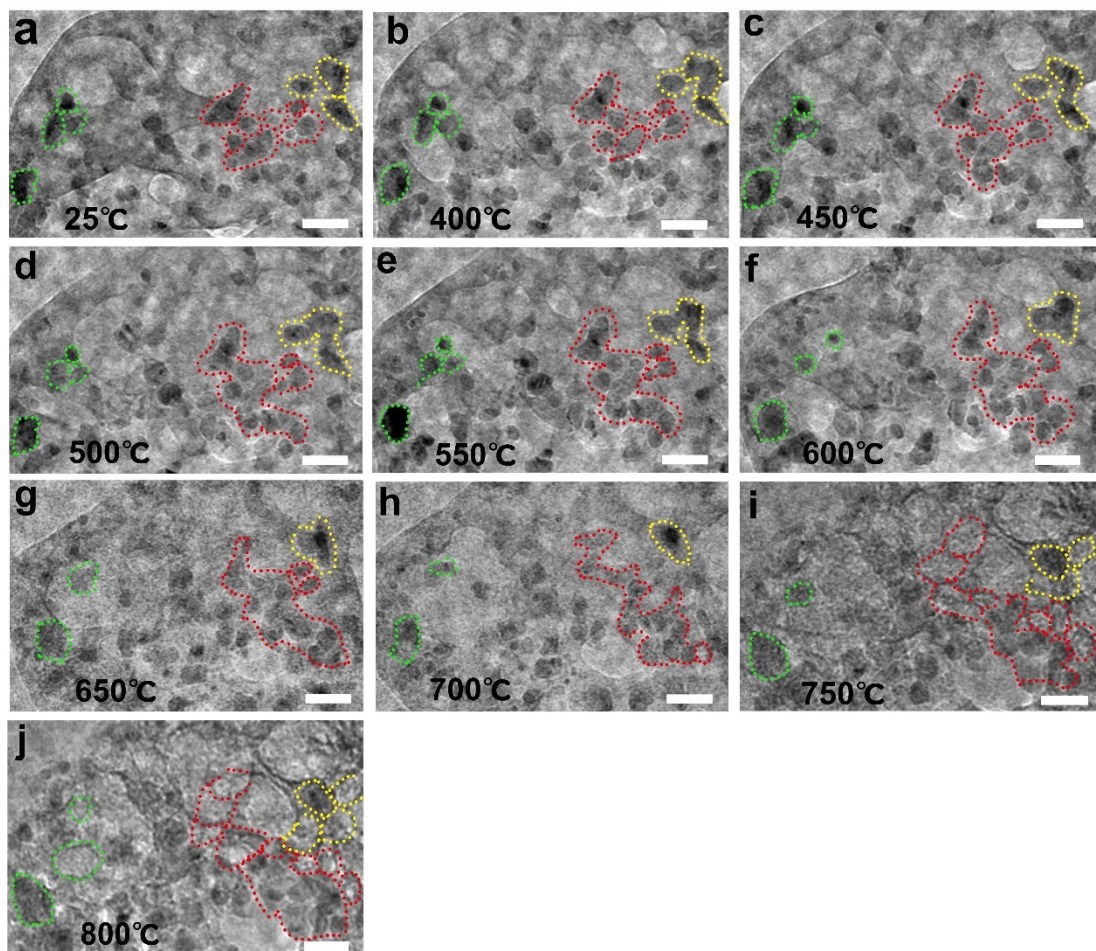


Figure S11. *In-situ* TEM study of the formation of VNGNMAs. Images a-j show the formation processes of hollow graphene wall pores when the original positions of Ni nanoparticles at high temperatures were close to each other. Scale bars, 20 nm.

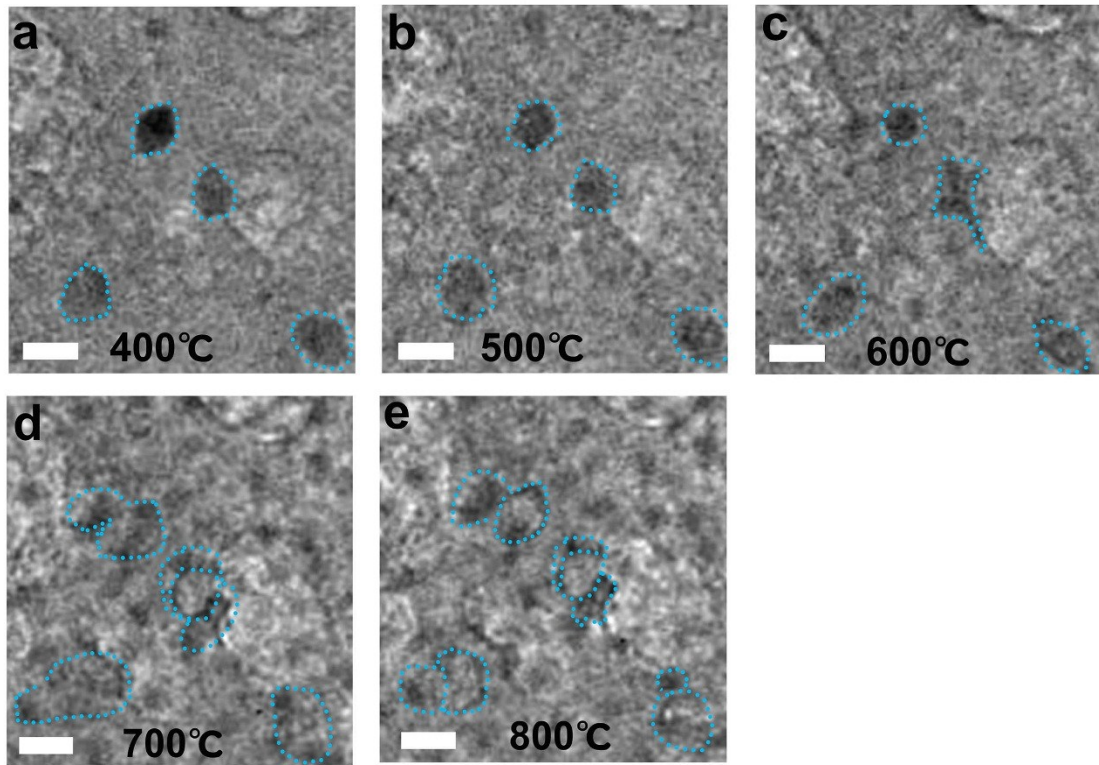


Figure S12. *In-situ* TEM study of the formation of VNGNMAs. Images a-j show the formation processes of hollow graphene wall pores when the original positions of Ni nanoparticles at high temperatures were far away from each other. Scale bars, 20 nm.

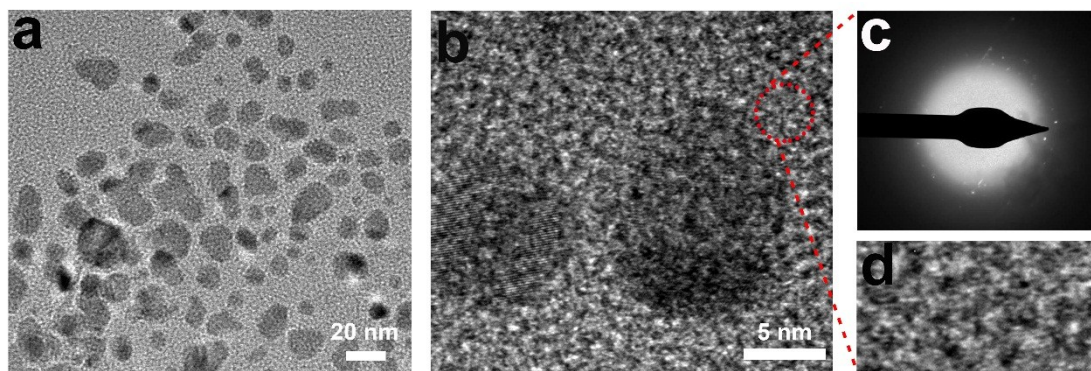


Figure S13. TEM, HRTEM images and SAED patterns of samples were annealed at 400°C.

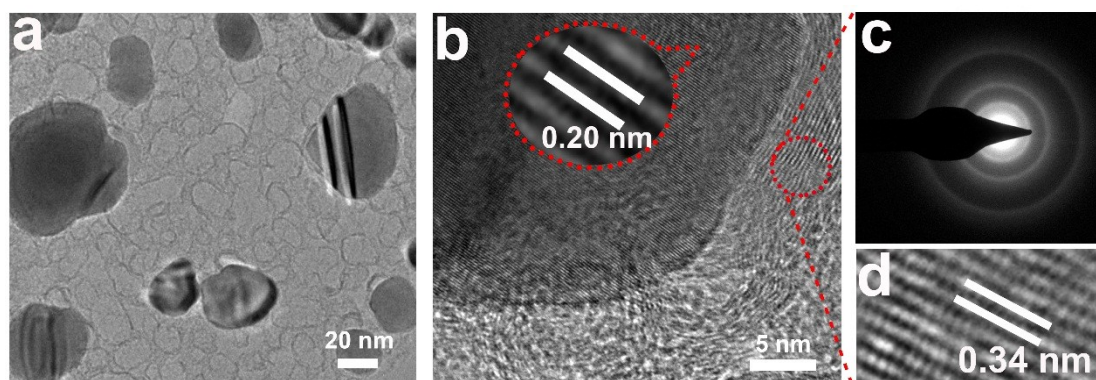


Figure S14. TEM and HRTEM images and SAED patterns of samples were annealed at 800°C.

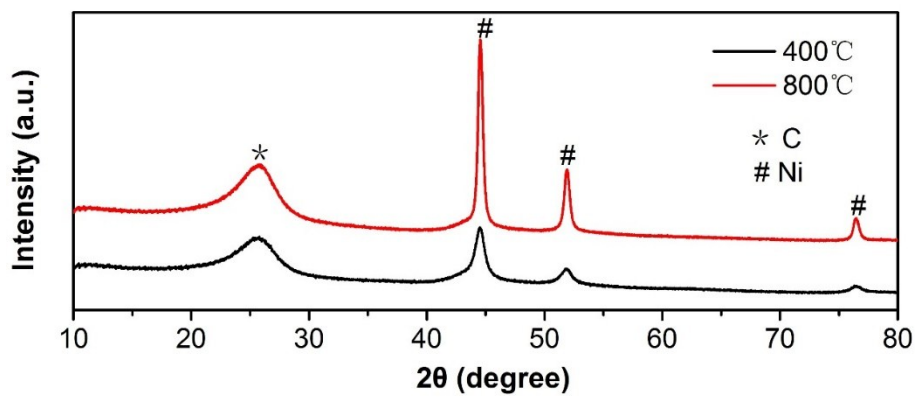


Figure S15. The XRD patterns of the 400 and 800 °C treatment samples based on carbon cloth.

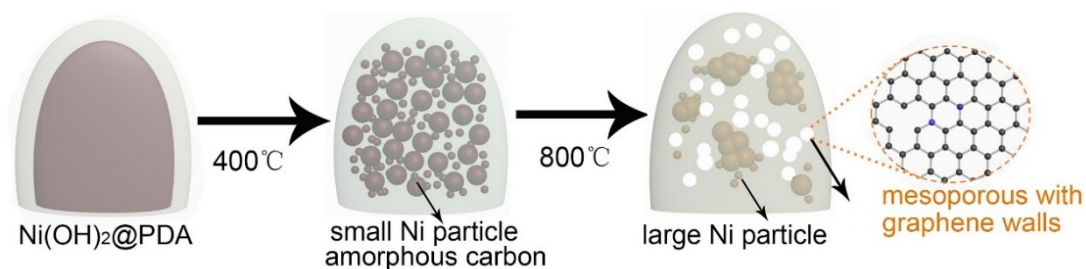


Figure S16. Staged heating process of the VNGNMAs.

The morphology of sample at initial (400 °C) and final temperature (800 °C) of this heating process are further characterized by TEM at different magnifications. Figure S13a and S13b clearly show that the small Ni particles are surrounded by carbon species after heating at 400°C. It can be observed that there is no diffraction ring in selected-area electron-diffraction (SAED) patterns in Figure S13c, which indicates that amorphous carbon is formed from the carbonization process of PDA at 400 °C. This is consistent with the HRTEM image in Figure S13d. Significantly, the small Ni particles merged into large ones and amorphous carbon transformed into crystalline carbon with numerous pores when heated to 800 °C (Figure S14a,b). The sizes of Ni nanoparticles obtained at 400 and 800 °C were estimated by Scherrer equation from the broadening of characteristic peak in X-ray diffraction (XRD) pattern in Figure S15, in which the size at 800 °C is larger than that of 400 °C. This agrees well with the TEM data. The HRTEM image of the final sample obtained at 800 °C (Figure S14b, d) shows well-resolved lattice fringes with inter-planar distance of 0.20 and 0.34 nm, corresponding to the (111) plane of Ni and (002) plane of graphene, respectively. Moreover, the SAED pattern in Figure S14c also exhibits bright and sharp diffraction rings, implying the enhanced graphitization of amorphous carbon.

Our studies demonstrated that staged heating including low temperature stage and high temperature stage is crucial to the successful synthesis of VNGNMAAs (Figure S16). The low temperature stage can maintain the shape of the arrays and prevent the structure collapse in direct exposure to high temperatures. During this process, the Ni(OH)₂ was thermally decomposed into NiO and then reduced to small Ni particles by a carbothermal reduction reaction ($\text{NiO} + \text{C} \rightarrow \text{Ni} + \text{CO}_2\uparrow$ or $\text{CO}\uparrow$) simultaneously. At the high temperature stage, Ni particles can be easily approach each other via self-diffusion, adhere, and finally grow into a solid crystallite in sintering process. Owing to the high catalytic activity of the as-obtained Ni particles, the amorphous carbon transferred into high-quality graphene.

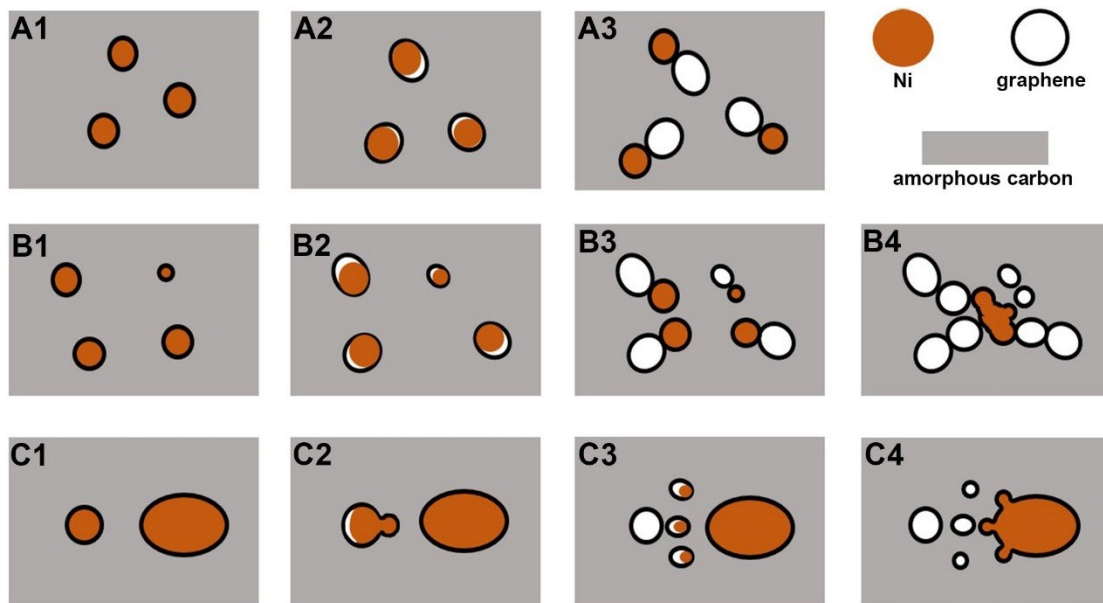


Figure S17. Illustration of three processes that form the pores of VNGNMAs.

Combined with real-time observation in the *in-situ* TEM, we propose a mechanism to explain the formation of nanopores, this can be described as diffusing-disembedding-graphitizing process of Ni particles embedded in amorphous carbon at high temperatures. Ni particles surrounded by amorphous carbon will display diffusion behavior due to the increase of surface energy at high temperature, where three events are observed at the same time:

(1) Isolated nanoparticles migrate from their original positions and produce holes (Figure S17 A1 ~ A3).

(2) Nearby nanoparticles migrate in Brownian-like motion and eventually merge into larger ones, leaving behind holes in their original position and migration path (Figure S17 B1 ~ B4).

(3) Ostwald ripening process of Ni nanoparticles. Large nanoparticles can grow at the expense of small ones when their size differences are significant. Smaller holes

are created by the exhaustion of small particles and the movement of mobile species
(Figure S17 C1 ~ C4).

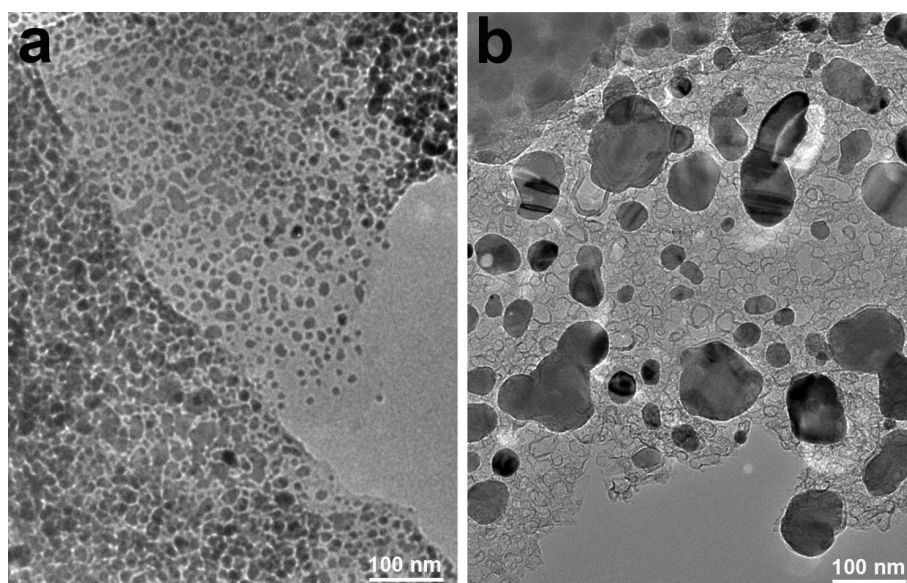


Figure S18. TEM of the (a) 400 and (b) 800 °C treatment samples.

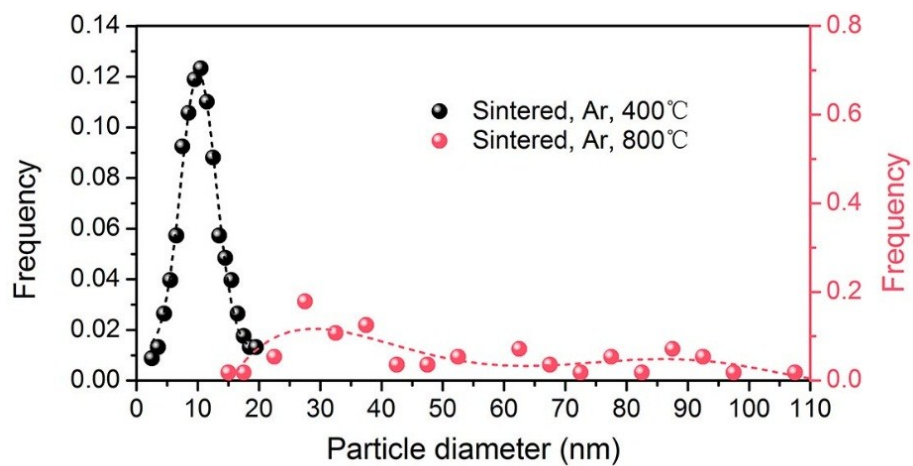


Figure S19. Size distributions of samples were annealed at 400°C and 800°C, respectively. According to the TEM images in figure S18.

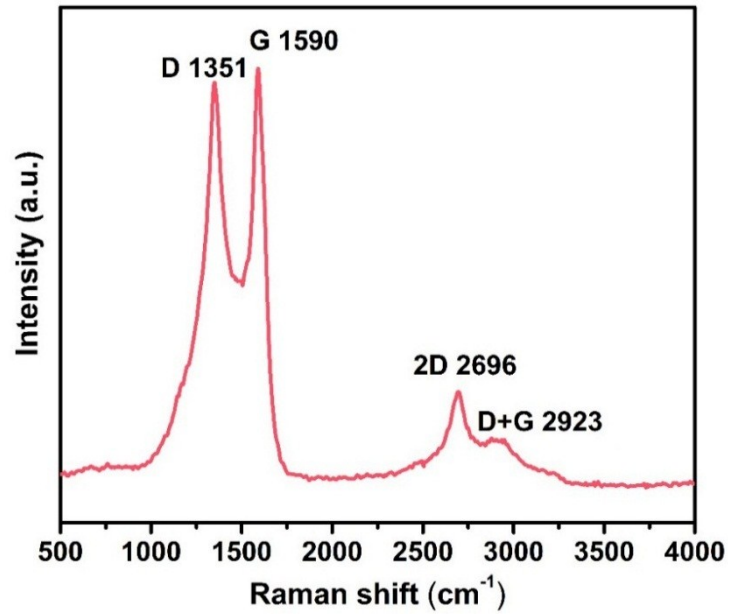


Figure S20. Raman spectrum of VNGNMAs. The Raman spectrum of VNGNMAs displays two characteristic peaks at 1,349 and 1,582 cm⁻¹ from the D and G bands of *sp*³ and *sp*² carbon, respectively. The abundant pores and edges in VNVGMAs are responsible for the high D band with the I_D/I_G ratio of 0.97. We also observe a sharp 2D band peak at 2696 cm⁻¹ (corresponding to an I_G/I_{2D} of 3.47). These evidences show that the presence of multilayer graphene features in VNGNMAs.

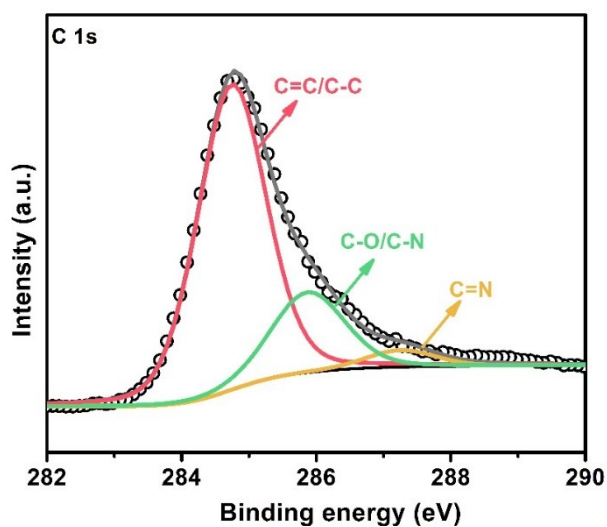


Figure S21. High-resolution C_{1s} XPS spectra of VNGNMA.

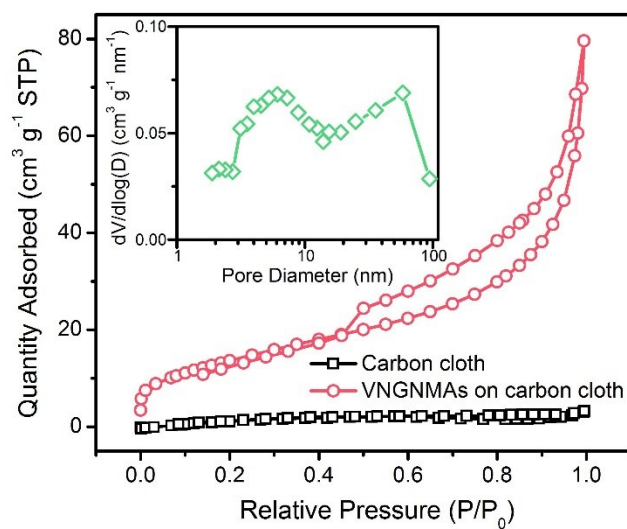


Figure S22. N_2 adsorption- desorption isotherms of CC@VNVGMAs and carbon cloth, inset is pore-size distribution of CC@VNGNMA.

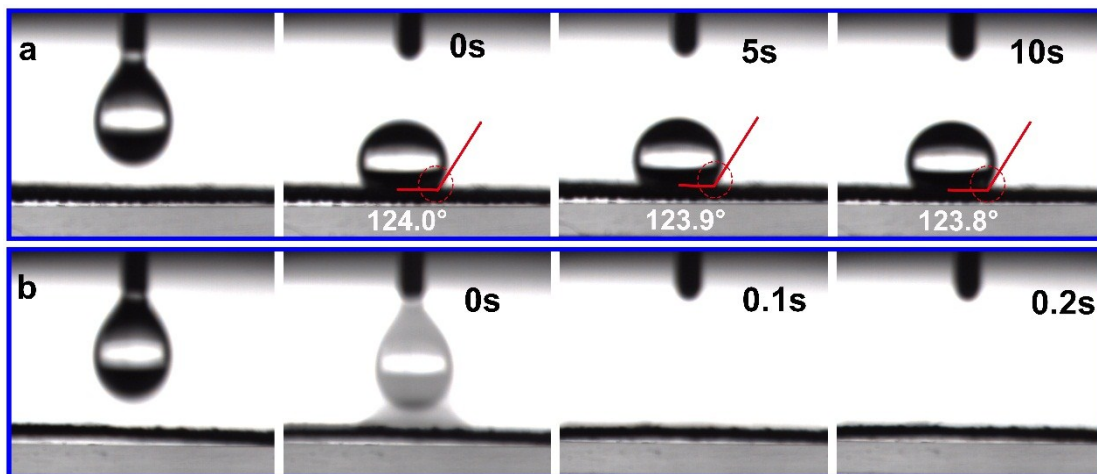


Figure S23. Water droplet on (a) Commercial carbon cloth and (b) VNGNMAs surface contact angle changes with time.

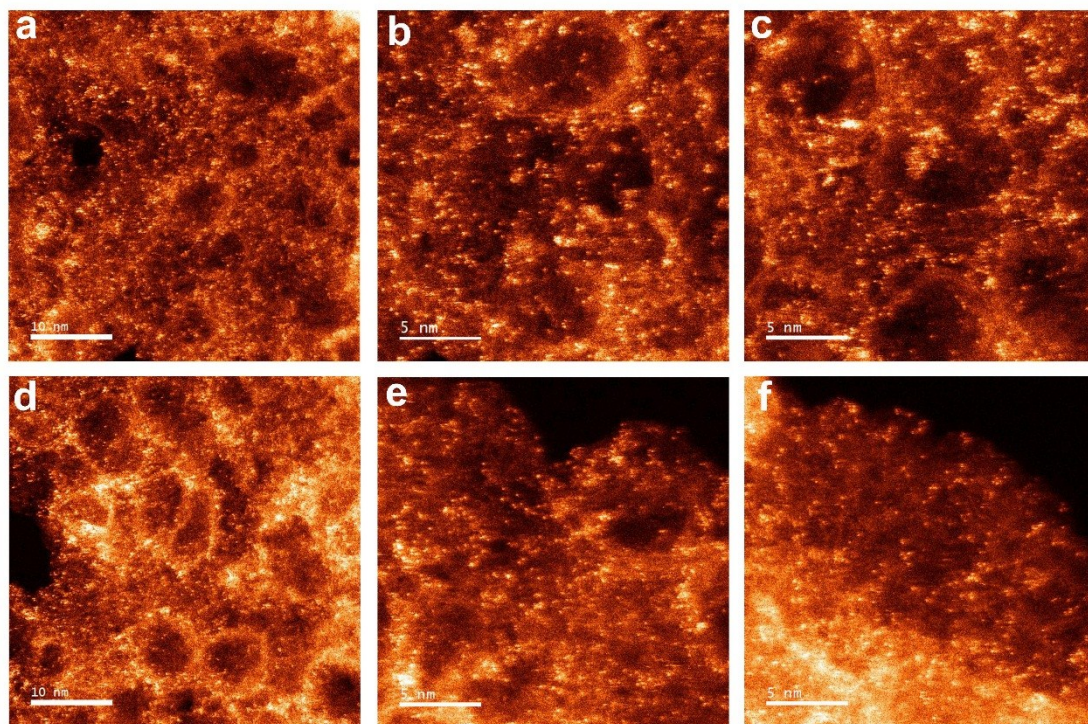


Figure S24. Representative STEM-ADF images of Pt₁ SAC-VNGNMA.

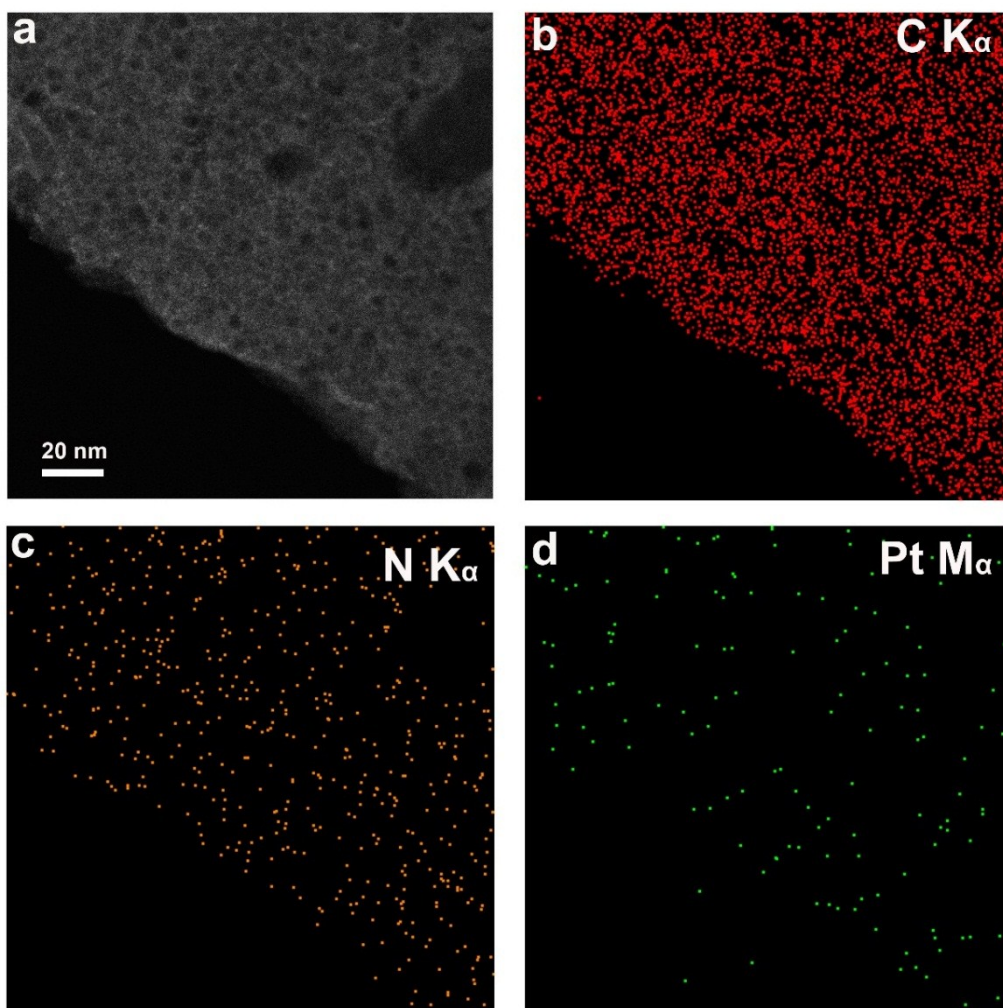


Figure S25. EDS mapping of Pt₁ SAC-VNGNMA.

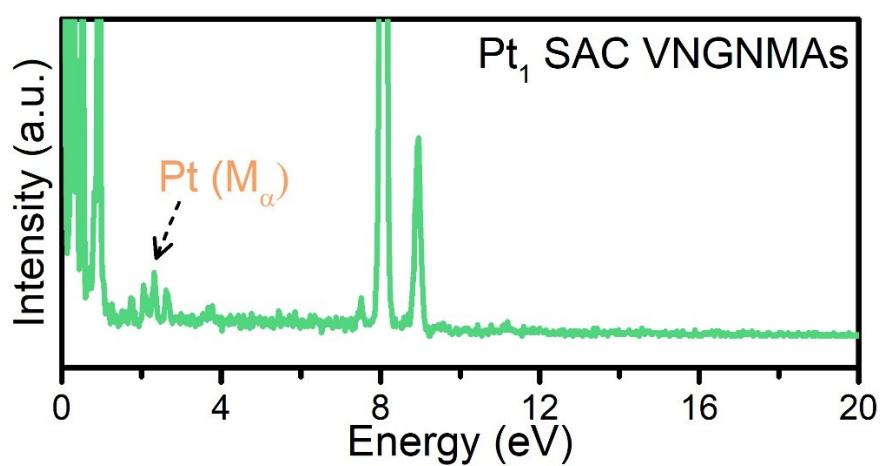


Figure S26. EDS spectra of Pt₁ SAC-VNGNMA.

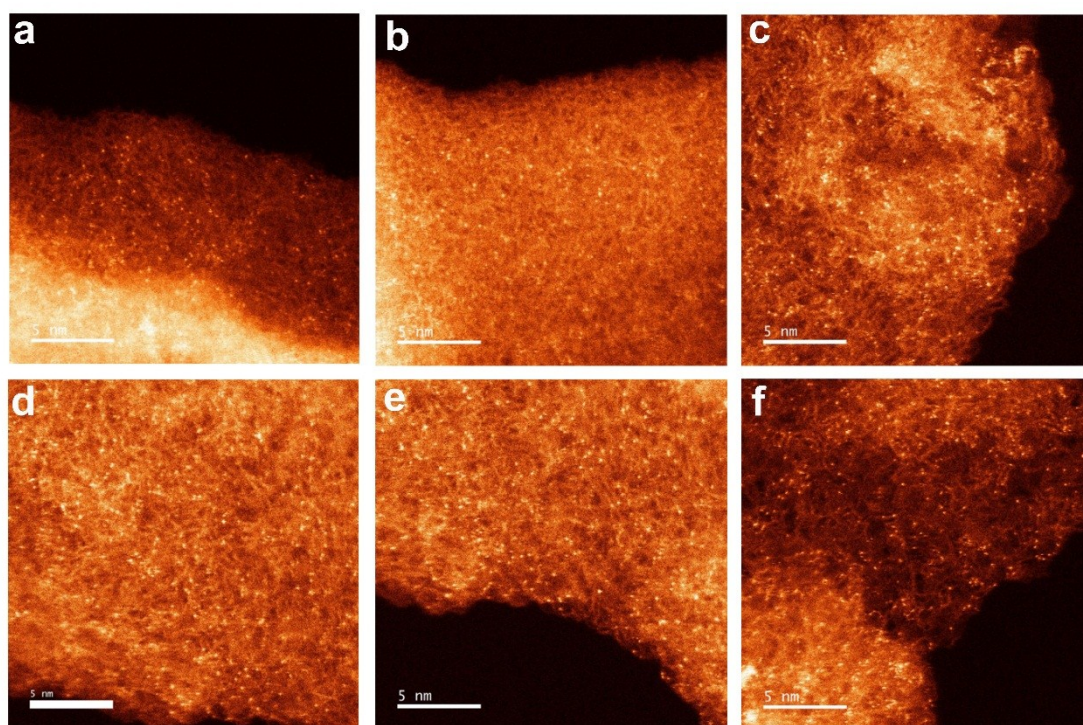


Figure S27. Representative STEM-ADF images of Pd₁ SAC-VNGNMAs.

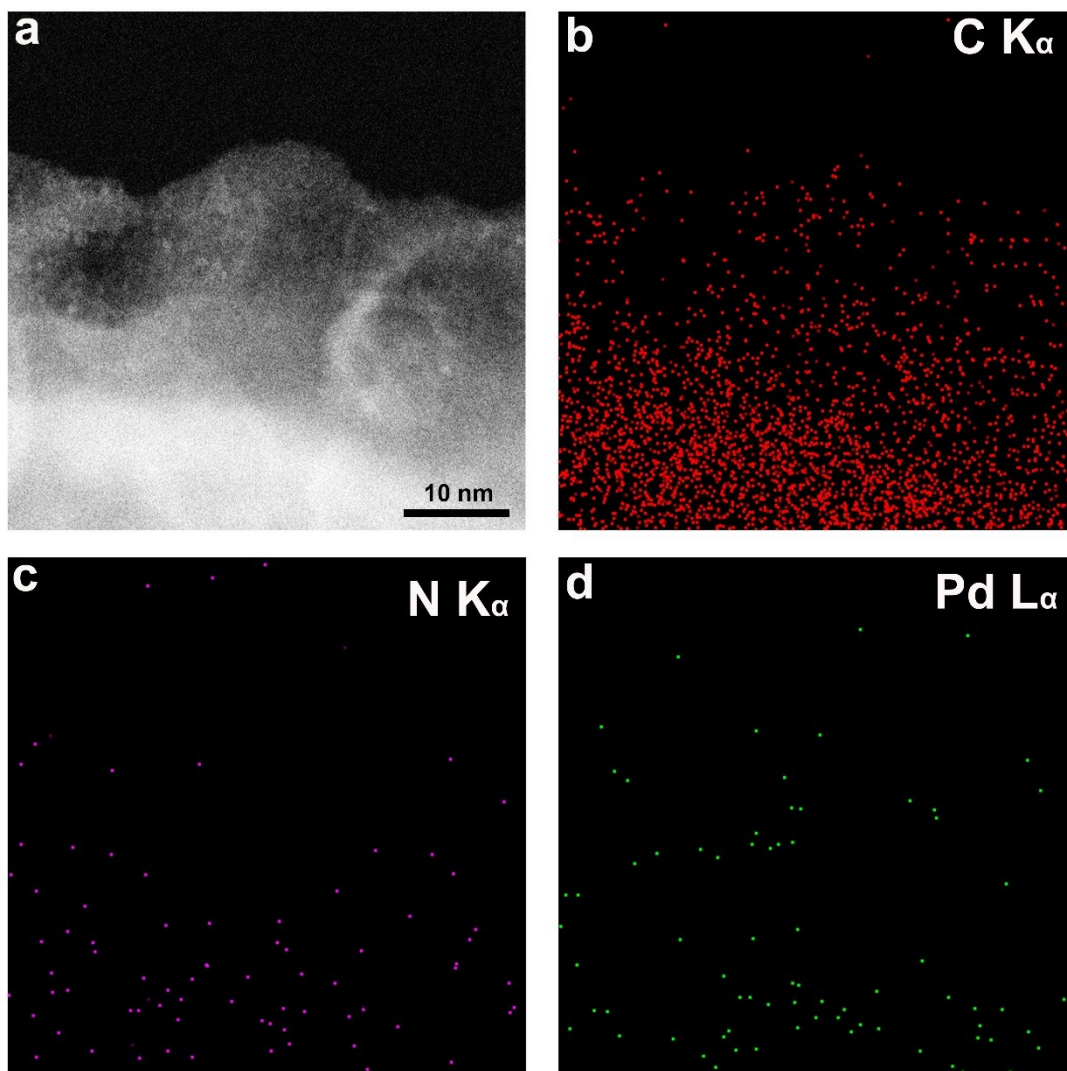


Figure S28. EDS mapping of Pd₁ SAC-VNGNMA.

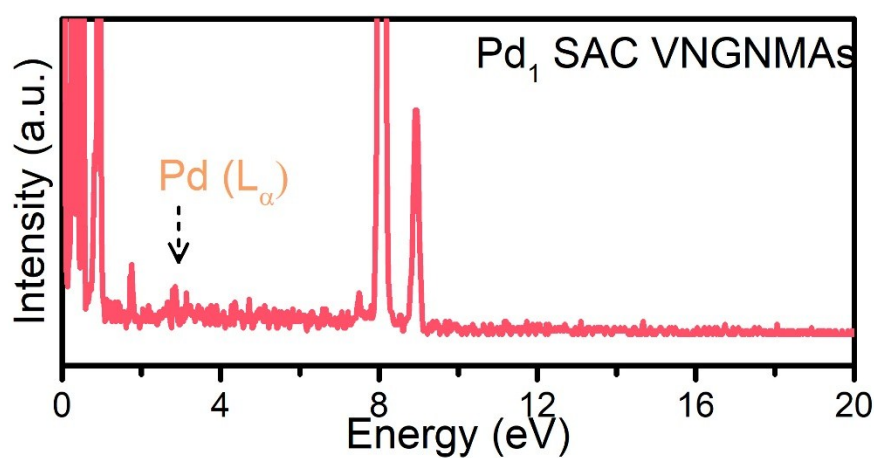


Figure S29. EDS spectra of Pd₁ SAC-VNGNMA.

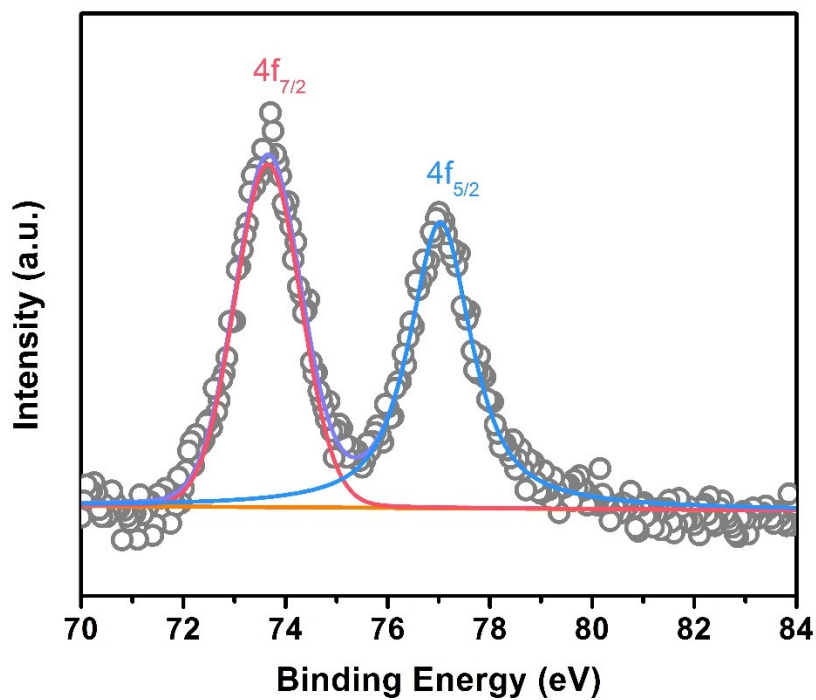


Figure S30. Pt 4f XPS spectra of Pt₁ SAC-VNGNMAs.

Two peaks with binding energies of 73.6 and 77 eV are observed in the Pt 4f XPS spectrum of Pt₁ SAC-VNGNMAs sample, indicating the formation of positively charged Pt species on VNGNMAs and the absence of Pt particle. (Ref. Zhang et al., Sci. Adv. 2018;4: eaao6657)

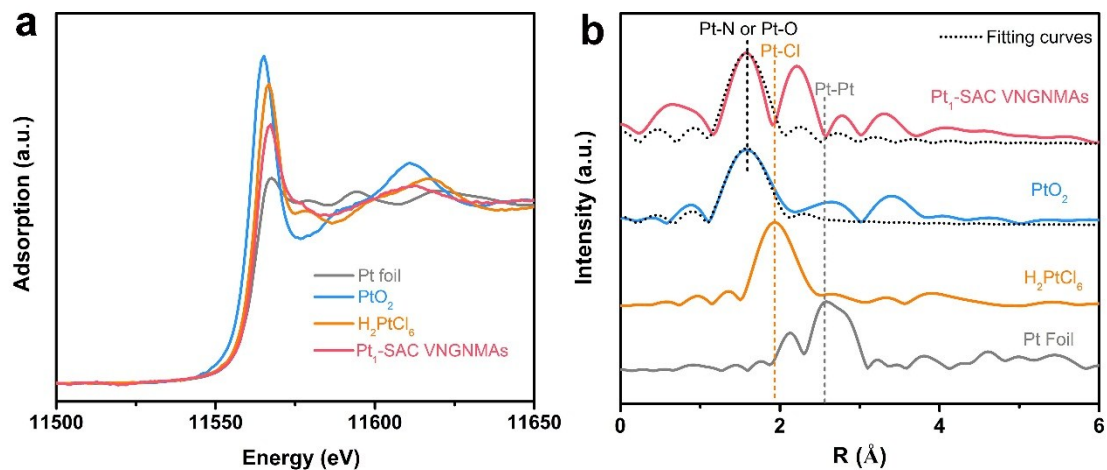


Figure S31. a, The normalized XANES spectra at the Pt L₃-edge and b, Fourier transforms of the Pt L₃-edge EXAFS oscillations of the Pt₁ SAC-VNGNMAs, H₂PtCl₆, PtO₂ and Pt foil.

Note: The peak at 2.0 ~ 2.5 Å can be attributed to the existence of ultrafine Pt clusters as our sample has been stored for months for available EXAFS measurements. However, the majority of Pt atoms remain in the single atom nature from the atomic resolution STEM-ADF images.

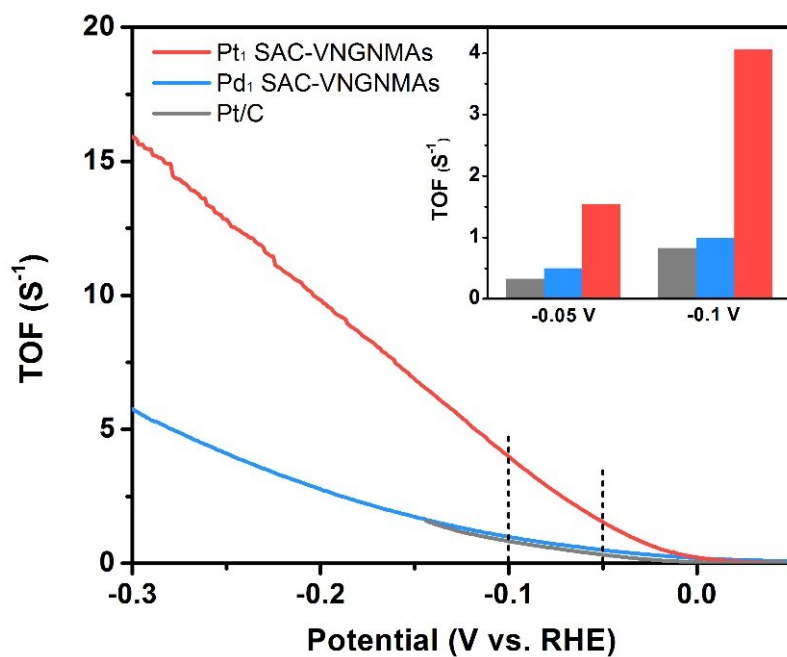


Figure S32. TOFs of Pt₁ SAC-VNGNMA_s, Pd₁ SAC-VNGNMA_s, and Pt/C catalysts at varied overpotentials.

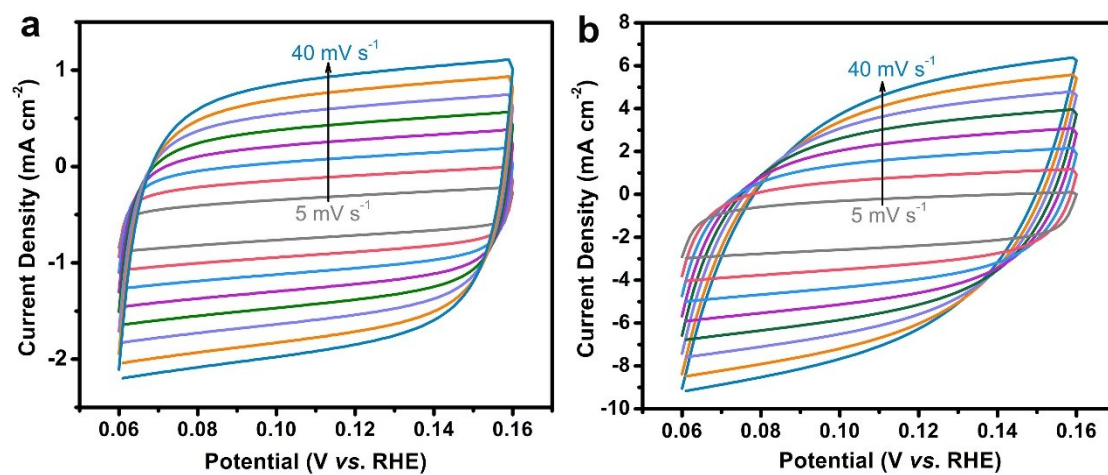


Figure S33. CV curves at different scan rates for the Pt₁ SAC-VNGNMA_s powder (a) and Pt₁ SAC-VNGNMA_s (b).

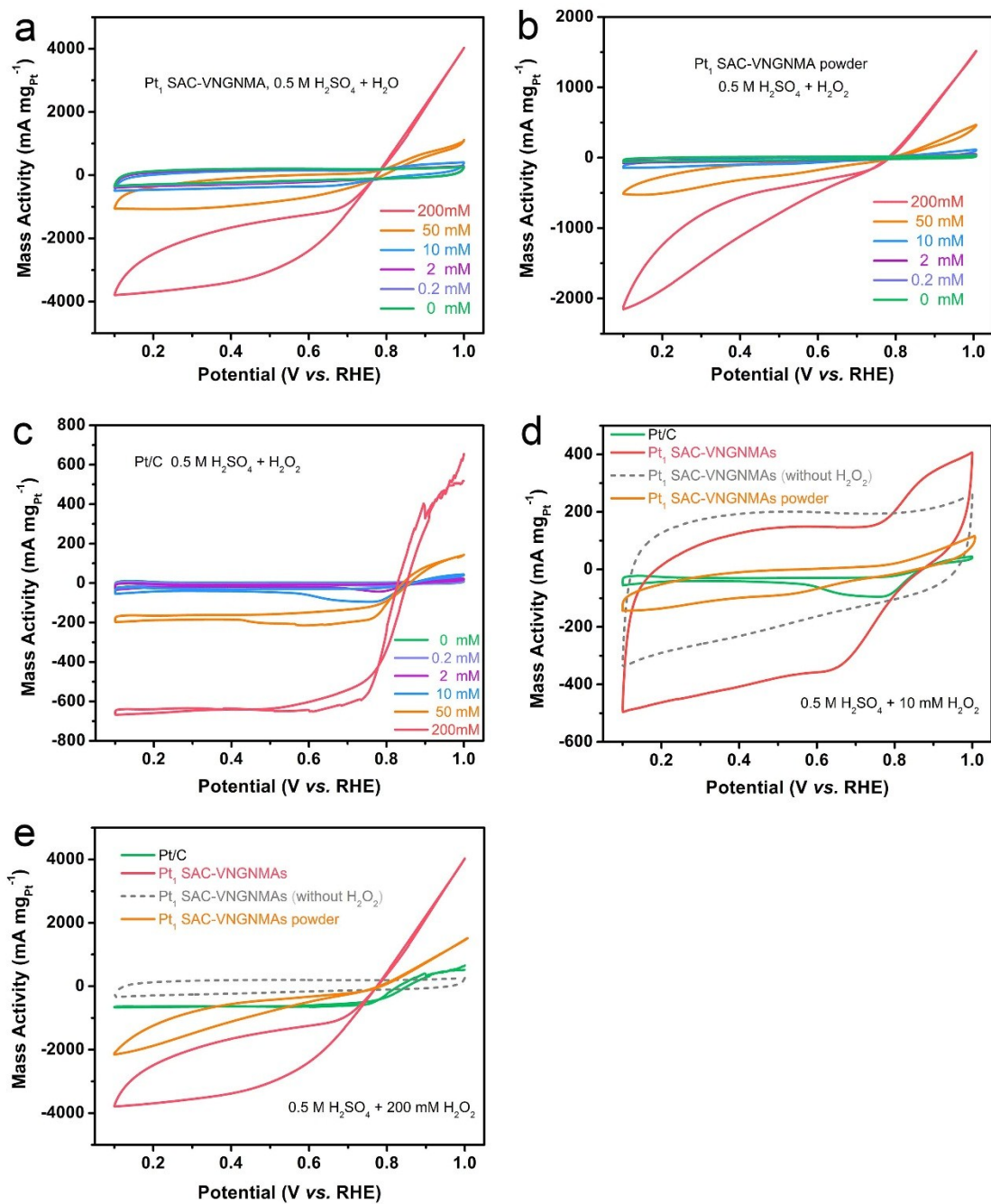


Figure S34. CV curves with different concentration of H₂O₂ in 0.5 M H₂SO₄ solution for Pt₁ SAC-VNGNMA (a), Pt₁ SAC-VNGNMA powder (b), and Pt/C (c), respectively. CV curves of Pt₁ SAC-VNGNMA, Pt₁ SAC-VNGNMA powder, and Pt/C in 0.5 M H₂SO₄ solution containing 10 mM (d) and 200 mM (e) H₂O₂, respectively.

Table S1. EXAFS data fitting results of PtO₂ and Pt₁ SAC-VNGNMAs.

Name	Bond	Number	σ^2	R	ΔE_0	R-factor
Pt ₁ SAC-VNGNMAs	Pt-N	1.4(\pm 0.3)	0.0034(\pm 0.001)	1.99(\pm 0.02)	12.98	0.03
PtO ₂	Pt-O	6.0	0.0012(\pm 0.0002)	2.01(\pm 0.02)	13.14	0.003

Table S2. HER performance comparison of noble metal-based catalysts in acid solutions.

	Catalyst	η_{10} (mV)	η_{100} (mV)	Tafel slope (mV/dec)	Reference
1	Pt₁ SAC-VNGNMAs	15	110	49	This work
2	Ru@C ₂ N	22	-	30	<i>Nat. Nanotechnol.</i> 2017, 12 , 441
3	Pt-MoS ₂	51	-	40	<i>Nat. Commun.</i> 2013, 4 , 1444
4	CuPdPt/C	55	95	25	<i>J. Mater. Chem. A</i> , 2016, 4 , 15309
5	Pt/BCF	55	-	32	<i>Catal. Today</i> 2016, 262 , 141
6	Pt@NHPCP	57	-	27	<i>Nano Energy</i> , 2017, 40 , 88
7	Pt ₂ Pd/NPG	58	-	68	<i>Carbon</i> . 2017, 114 , 740
8	PdCu@Pd	68	140	35	<i>ACS Appl. Mater. Interfaces</i> 2017, 9 , 8151
9	Au-Cu/CNF	83	-	74	<i>ACS Appl. Mater. Interfaces</i> 2017, 9 , 19756
10	Ag@PdAg	93	195	70	<i>Nano Energy</i> , 2017, 34 , 306
11	Au/NC	130	-	76.8	<i>Angew. Chem. Int. Ed.</i> 2016, 55 , 8416
12	Pd-Cu-S	58	-	35	<i>J. Mater. Chem. A</i> , 2017, 5 , 18793
13	Pd-Mn ₃ O ₄	14	200	42	<i>Chem. Commun.</i> , 2016, 52 , 6095
14	PtCoFe@CN	45	-	32	<i>ACS Appl. Mater. Interfaces</i> 2017, 9 , 3596

Table S3. Comparison of Selected State-of-the-Art SACs for HER in 0.5 M H₂SO₄.

	Catalyst	η_{10} (mV)	η_{100} (mV)	Tafel slope (mV/dec)	Reference
1	Pt₁ SAC- VNGNMAs	15	110	49	This work
2	Mo ₁ N ₁ C ₂	132	-	90	<i>Angew. Chem. Int. Ed.</i> 2017, 56, 16086
3	Pt@PCM	105	-	65.3	<i>Sci. Adv.</i> 2018, 4, eaao6657
4	Co-NG	147	-	82	<i>Nat. Commun.</i> 2015, 6, 8668
5	A-Ni-C	34	112	41	<i>Nat. Commun.</i> 2016, 7, 10667
6	Pt/NGNs	39	-	29	<i>Nat. Commun.</i> 2016, 7, 13638
7	Ni-doped Graphene	150	-	45	<i>Angew. Chem. Int. Ed.</i> 2015, 54, 14031
8	Pt-MoS ₂	150	-	96	<i>Energy Environ. Sci.</i> , 2015, 8, 1594
9	SWNT/Pt	27	130	38	<i>ACS Catal.</i> 2017, 7, 3121
10	A-Ni@DG	~270	-	47	<i>Chem.</i> 2018, 4, 285
11	CoN _x /C	133	-	57	<i>Nat. Commun.</i> 2015, 6, 7992.
12	PtSA-NT-NF	24	88	30	<i>Angew. Chem. Int. Ed.</i> 2017, 56, 13694
13	Ru SAs@PN	24	~100	38	<i>Angew. Chem. Int. Ed.</i> 2018, 57, 9495
14	Pt@MoS ₂ /NiS ₂	~46	~100	40	<i>Small</i> 2018, 14, 1800697
15	Pt ₁ @Fe-N-C	60	-	42	<i>Adv. Energy Mater.</i> 2018, 8, 1701345
16	CoNC-Cl	130	-	41	<i>Adv. Mater.</i> 2017, 29, 1703436.